AMSI SUMMER RESEARCH SCHOLARSHIPS 2025–26

Get a taste for Research this Summer

Dynamic Stiffening of Flexible Microswimmers

Joshua Borsky

Supervised by A/Prof. Douglas Brumley

The University of Melbourne

Jane Street®

AMSI AUSTRALIAN MATHEMATICAL SCIENCES INSTITUTE

Abstract

Marine bacteria typically use a single *flagellum*—a thin, propeller-like appendage—to move through ocean waters. Experimental work concerning the motion of these bacteria has shown that the *hook* connecting a bacterium's flagellum and cell body can buckle under force, allowing the bacterium to adjust its orientation. Notably, this turn strategy relies on varying the stiffness of the connective hook over time. In this report, we extend existing models of flexible microswimmers to include a simplified model of this dynamically changing stiffness. Due to the introduction of a new timescale for the stiffening of the flagellar hook, a new dimensionless group emerges which is shown to have a roughly linear relationship with turn angle, suggesting that variation of this parameter may well account for small changes in average deflection angle observed in bacteria migrating towards desirable chemicals. A key dimensionless group examined in earlier research—a normalised stiffness of the flagellar hook—is reproduced by this study, alongside other parameters concerning the geometry, propulsive force and resistivity of the swimmer. A critical value of this first parameter at which a buckling bifurcation occurs is recreated in the dynamic setting, and its impact on swimming modes is analysed with reference to final deflection angle using numerical simulations. Furthermore, two new critical thresholds for this normalised stiffness are uncovered that describe the behaviour of the dynamically stiffening swimmer in greater detail. We demonstrate the dependence of these critical thresholds on the body geometry and flagellum length, highlighting the role of morphology in governing motility and the potential for a broad variety of behaviours within and between species of marine bacteria.

1 Introduction

The obstacles to motion at the microscopic length scales of bacteria are distinct to those faced by macroscopic organisms (Qiu et al. (2014)). In environments where the *Reynolds number*—a ratio Re of inertia against viscosity—is very small, conservation of momentum can be considered effectively absent. In particular, under the limiting assumption that $\mathrm{Re} = 0$ (which characterises the regime of *Stokes flow*), fluid motion is time-independent and will instantly return to motionlessness in the absence of applied force. One famous consequence of this fact is the *Scallop Theorem* of Purcell (1977), which dictates that no motion that looks identical when 'played in reverse' can generate net displacement.

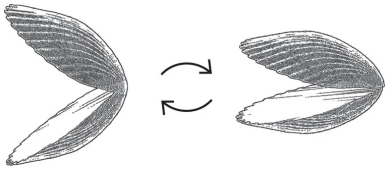

Figure 1: A scallop's reciprocal motion, from Qiu et al. (2014)

To overcome this restriction, marine bacteria propel themselves via the rotation of a helical (i.e. chiral) appendage called a *flagellum*, whose rotation counter/clockwise can generate thrust in either the forward or backward direction. Xie et al. (2011) found that in order to reorient off-axis, these bacteria employ a *run-reverse-flick* strategy illustrated in Figure 3 to follow; after a short run in the direction of its flagellum, a bacterium will reverse the direction of its propulsion, at which point it undergoes a 'flick' that allows it to change direction off axis. Later experimental work by Son et al. (2013) on the species *V. alginolyticus* showed that the mechanism for this flick is a mechanical buckling instability of the connective *hook* between a bacterium's flagellum and cell body, due to compression resulting from hydrodynamic drag (as shown in Figure 2).

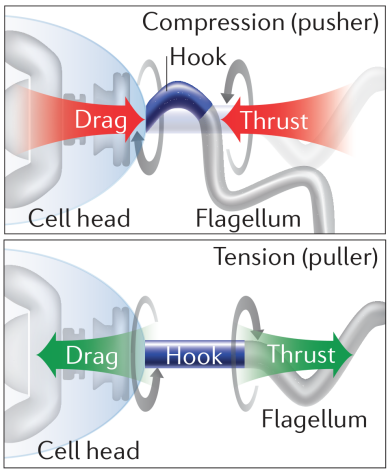

Figure 2: Illustration of hook buckling, from Son et al. (2013)

The buckling of this flagellar hook results in a roughly right-angle turn (Son et al. (2013)), and varying this turn angle and the frequency of reorientations is a primary mechanism of *chemotaxis*—the preferential motion of a microorganism according to chemical gradients (Sourjik & Wingreen (2012)) which is crucial to their viability. As such, a detailed understanding of orientation angle and frequency, as well as their variation under differing physical and environmental conditions, is key to a deeper understanding of marine ecology. Notably, this turning-by-buckling strategy relies on a varying bending stiffness of the flagellar hook that weakens dynamically during a reorientation event (Son et al. (2013)). Past work by Nguyen & Graham (2017) has modelled this behaviour with a hook of constant bending stiffness, and an extension by Jabbarzadeh & Fu (2018) saw the hook modelled as a Kirchoff rod; nevertheless, neither study was able to recreate the flick observed in experiments with hook flexibility alone. In this report, we extend existing models of this turning-by-buckling behaviour to include a simplified model of dynamically changing hook stiffness. We aim to gain an understanding of the physical parameters that govern eventual turn angle in the flick event, in order to account for the variation in turn angle that occurs during chemotaxis, and predict how microswimmers might react to different conditions. In Section 3, we describe our physical model and use it to derive equations of motion. With these equations, we perform in Section 4 dynamical analysis to predict critical thresholds for our system. Finally, in Sections 5 and 6 we simulate reorientation events numerically and explain our results using the thresholds derived prior.

2 Statement of Authorship

The results contained within this report are the work of Joshua Borsky under direct supervision of A/Prof. Douglas Brumley. This work aims to extend to the 'Dynamic Toy Model' put forward by Nguyen & Graham (2017), and as such examines a closely related model. Furthermore, Son et al. (2013) constitutes the main source of biological knowledge for this research.

3 Model Setup

In this section we construct our model for the bacterium in motion, and use it to set up a system of ODEs for simulations. Subsections 3.1 and 3.2 respectively detail the physical dimensions and forces/torques that constitute the model itself, while Subsections 3.3, 3.4 and 3.5 use techniques from low-Reynolds fluid mechanics and dynamical analysis to derive our system of ODEs. Finally in Subsection 3.6 we use existing biological literature to provide reasonable parameter ranges for our study.

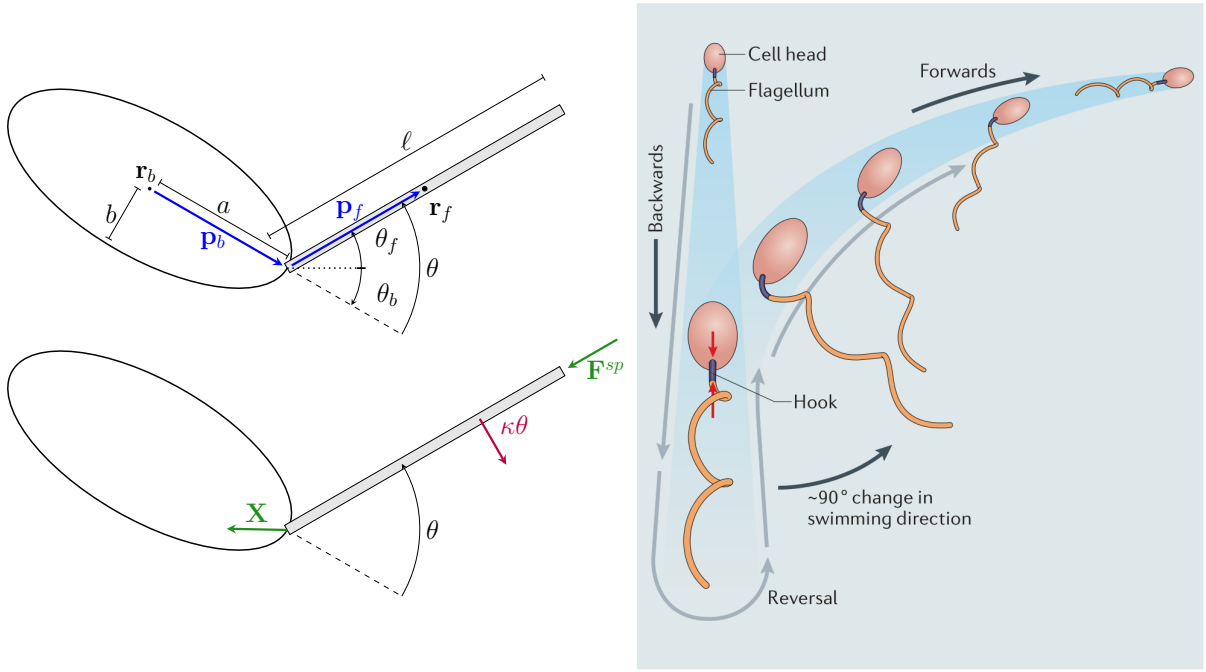

Figure 3: Schematic of the model examined in this report, compared with full bacterial geometry. Top left: positions, orientations and dimensions. Bottom left: imposed forces and torques. Right: Illustration of run-reverse-flick motility, from Son et al. (2015).

3.1 Body Dimensions

We begin by detailing the physical quantities that comprise our model, depicted in Figure 3. We model the flagellar hook as a torsion spring connecting two rigid components. In particular, following the 'Dynamic Toy Model' put forward by Nguyen & Graham (2017), we model the body as a prolate spheroid (with semimajor and semiminor axes a and b respectively) and the flagellum as a cylinder of length ℓ. This setup simplifies the intricate hook geometry (Kato et al. (2019), Nord et al. (2022)) and the finite bending rigidity of the flagellum (Takano et al. (2003)); however, the negligible size of the hook (Koike et al. (2010)) and the comparatively large stiffnesses of the flagellum justify these simplifications. Indeed, modelling work by Jabbarzadeh & Fu (2018) extending Nguyen & Graham (2017) by considering the hook as a Kirchoff rod was unable to recreate buckled behaviour without significant flagellar flexibility; in offering a model more agnostic to the internal mechanics of the hook, we aim to more easily recreate observed behaviours with lower computational cost. To keep track of the locations and orientations of each component, we define the points $\mathbf{r}_i$ and unit vectors $\mathbf{p}_i$, and the angles θ_i corresponding to each vector, where we use $i = b,\ f$ to denote components corresponding to the body and flagellum respectively. Finally, we write $\theta = \theta_f - \theta_b$ $(= \pm \arccos(\mathbf{p}_f \cdot \mathbf{p}_b))$ for the deflection angle between body and flagellum.

3.2 Imposed Forces and Torques

We detail here the external (non-hydrodynamic) forces that will govern the swimmers motion. Still following Nguyen & Graham (2017), we simulate flagellar thrust with the addition of a self propulsive point force $\mathbf{F}^{\text{sp}} = -\mathbf{p}_f F^{\text{sp}}$ realised at the end the flagellum. This imposition compensates for the simplified model of the flagellum as an axisymmetric cylinder; flagellar propulsion in reality relies on the torque-velocity coupling of its chiral helix structure (Lauga & Powers (2008)). Nevertheless, this simplified methodology proposed by Nguyen & Graham (2017) was able to recreate much of the buckling behaviour sought, with results diffffering slightly from their full three-dimensional simulations. We also retain the constraint force $\mathbf{X}$ ensuring the connectedness of the components, and the restoring torque $\kappa\theta$ on both components realised from the position of the connection $\mathbf{r}_c := \mathbf{r}_b + a\mathbf{p}_b$. We do not prescribe the magnitude or direction of the former, but rather will calculate it using the force balance conditions that generate our governing equations.

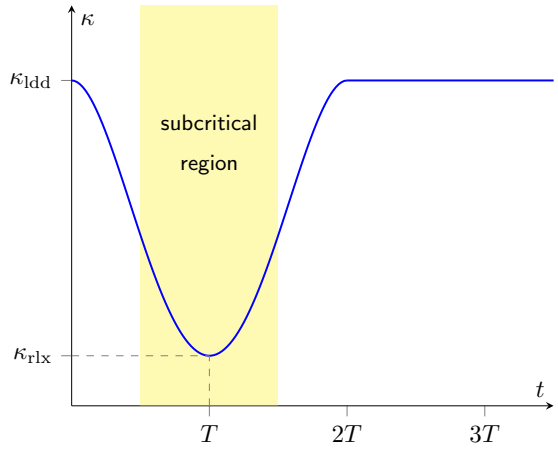

$$\kappa = \begin{cases} \kappa_{\text{ldd}}, & t < 0 \text{ or } t > 2T \\ \kappa_{\text{ldd}} + (\frac{t}{T})^2(\frac{t}{T} - 2)^2(\kappa_{\text{rlx}} - \kappa_{\text{ldd}}), & 0 \leq t \leq 2T \end{cases}$$

Figure 4: Dynamic stiffening of flagellar hook. κ_{ldd} and κ_{rlx} are the loaded and relaxed (i.e. maximal and minimal) values of the spring constant, t is the time in seconds from the beginning of the reversal event and T is a new timescale representing the time taken for the hook to unroll completely. Yellow highlighted region of graph is the region in which κ drops below the buckling threshold outlined by Nguyen & Graham (2017)

This study's addition to the model is the dynamic un/stiffening of the spring constant κ, according to the expression detailed in Figure 4. A piecewise quartic function was chosen to allow differentiability at the end points, an intuitively reasonable assumption given the hypothesised (Son et al. (2013)) role of hook un/twisting as the mechanism for this change in spring constant, but a more detailed understanding of the hook's dynamics is necessary to fully evaluate the validity of this expression; see Nord et al. (2022) and Kato et al. (2019) for inspiration on more detailed modelling of the hook. Piecewise linear and piecewise parabolic expressions with similar trajectories were also trialled, with no significant effect on final angle or trajectory. The time-dependent spring constant κ will allow the microswimmers in this model to exhibit both buckled, subcritical behaviour and straightened, supercritical behaviour as κ changes over the course of a single reorientation event, giving rise to the flick observed in *V. alginolyticus* and other uniflagellate bacteria.

3.3 Derivation of Governing Equations

We proceed now with the derivation of our governing equations. The force/torque balance conditions on a body in Stokes flow (Kim & Karrila (1991)) form the basis for our derivation, which we notate as follows:

$$\mathbf{F}_i^{\mathrm{h}} + \mathbf{F}_i^{\mathrm{ext}} = \mathbf{0}$$
$$\mathbf{T}_i^{\mathrm{h}} + \mathbf{T}_i^{\mathrm{ext}} = \mathbf{0}$$

Supplementing this condition with the resistance/mobility tensor framework for a general body in unbounded Stokes flow in quiescent fluid (Kim & Karrila (1991))

$$\begin{pmatrix} \mathbf{F}_i^{\mathrm{h}} \\ \mathbf{T}_i^{\mathrm{h}} \end{pmatrix} = - \begin{pmatrix} \mathbf{A_i} & \mathbf{B_i} \\ \mathbf{B_i} & \mathbf{C_i} \end{pmatrix} \cdot \begin{pmatrix} \dot{\mathbf{r}}_i \\ \omega_i \end{pmatrix}$$

we can derive a complete set of governing equations for our system. Axisymmetry of each component gives (Kim & Karrila (1991))

$$\mathbf{A}_i = A_i^{\parallel}\mathbf{p}_i\mathbf{p}_i + A_i^{\perp}(\mathbf{I} - \mathbf{p}_i\mathbf{p}_i), \qquad \mathbf{B}_i = \mathbf{0}, \qquad \mathbf{C}_i = C_i^{\parallel}\mathbf{p}_i\mathbf{p}_i + C_i^{\perp}(\mathbf{I} - \mathbf{p}_i\mathbf{p}_i)$$

for some scalars $A_i^{\perp}, A_i^{\parallel}, C_i^{\perp}, C_i^{\parallel}$ where $\mathbf{I}$ is the identity 2-tensor and $\mathbf{n} = \frac{\mathbf{p}_b \times \mathbf{p}_f}{\|\mathbf{p}_b \times \mathbf{p}_f\|}$. $\mathbf{B}$ vanishing removes the torque-velocity coupling of the system, and so in the absence of any applied torque we need only consider in-plane motion of the microswimmer, with the simplified relationships

$$A_i^{\perp}(\mathbf{I} + (\tfrac{1}{\alpha_i} - 1)\mathbf{p}_i\mathbf{p}_i) \cdot \dot{\mathbf{r}}_i = \mathbf{F}_i^{\mathrm{ext}}, \qquad C_i\dot{\theta}_i = \mathbf{T}_i^{\mathrm{ext}},$$

where $\alpha_i = \frac{A_i^{\perp}}{A_i^{\parallel}}$ and $C_i = C_i^{\perp}$. Our governing equations are then fully specified by the imposed forces and torques on the swimmer:

$$\begin{aligned} \dot{\mathbf{r}}_i &= \tfrac{1}{A_i^{\perp}}(\mathbf{I} + (\tfrac{1}{\alpha_i} - 1)\mathbf{p}_i\mathbf{p}_i)^{-1} \cdot ((-1)^{\delta_{if}}\mathbf{X} - \delta_{if}\mathbf{F}^{sp}) \\ &= \tfrac{(-1)^{\delta_{if}}}{A_i^{\perp}}(\mathbf{I} + (\alpha_i - 1)\mathbf{p}_i\mathbf{p}_i) \cdot (\mathbf{X} + \delta_{if}F^{sp}\mathbf{p}_f) \qquad (1) \\ \dot{\theta}_i &= \tfrac{1}{C_i}((-1)^{\delta_{if}}\kappa(\theta_f - \theta_b) + ((-1)^{\delta_{if}}a_i\mathbf{p}_i \times (-1)^{\delta_{if}}\mathbf{X}) \cdot \mathbf{n}) \\ &= \tfrac{1}{C_i}((-1)^{\delta_{if}}\kappa(\theta_f - \theta_b) + (a_i\mathbf{p}_i \times \mathbf{X}) \cdot \mathbf{n}) \qquad (2) \\ \mathbf{r}_f &= \mathbf{r}_b + a\mathbf{p}_b + \tfrac{\ell}{2}\mathbf{p}_f \qquad (3) \end{aligned}$$

where δ_{ij} is the Kronecker Delta, $a_b = a, a_f = \frac{\ell}{2}$, and (3) is an algebraic condition imposing that flagellum and body remain connected.

3.4 Resistivity Coefficients

We use resistive force theory to obtain values for the resistive coefficients in equations (1) and (2). Because the bacterial body is modelled as a prolate ellipsoid, we can use the well known values from Kim & Karrila (1991) to determine

$$A_b^{\parallel} = \frac{16\pi\eta a e^3}{(e^2+1)\ln(\frac{1+e}{1-e}) - 2e}, \qquad A_b^{\perp} = \frac{32\pi\eta a e^3}{(3e^2-1)\ln(\frac{1+e}{1-e}) + 2e}, \qquad C_b = \frac{32\pi\eta a^3 e^3(2-e^2)}{3((e^2+1)\ln(\frac{1+e}{1-e}) - 2e)},$$

where $e = \sqrt{1 - b^2/a^2}$ is the eccentricity of the ellipse defining the spheroid. For the flagellum, we rely on the approximations by Nguyen & Graham (2017) based on the resistive force theory of Lighthill (1976) to approximate the truly helical flagellum by a cylinder, namely

$$\xi^{\perp}\ell := A_f^{\perp} = \eta\ell \sec\psi(\lambda^{\perp}\sin^2\psi + \lambda^{\parallel}\cos^2\psi), \qquad \xi^{\parallel}\ell := A_f^{\parallel} = \eta\ell\sec\psi(\lambda^{\perp} + \tfrac{\lambda^{\parallel}-\lambda^{\perp}}{2}\sin^2\psi),$$

$$C^{\perp} = \eta\ell\sin^2\psi\sec\psi\left[\frac{1}{2}(\tfrac{P}{2\pi})^2(\lambda^{\perp}\sec^2\psi + \lambda^{\parallel}) + \tfrac{4}{3}\ell^2(\lambda^{\perp}\csc^2\psi + \tfrac{\lambda^{\parallel}-\lambda^{\perp}}{2}))\right]$$

where

$$\lambda^{\perp} = \frac{4\pi}{\ln(\frac{0.18P}{r\cos\psi}) + \frac{1}{2}}, \qquad \lambda^{\parallel} = \frac{2\pi}{\log\frac{0.18P}{r\cos\psi} - \frac{1}{2}}$$

for a flagellum of pitch P, pitch angle ψ and filament radius r. We note that

$$C_f = \eta\ell\sin^2\psi\sec\psi\cdot\frac{1}{2}(\tfrac{P}{2\pi})^2(\lambda^{\perp}\sec^2\psi + \lambda^{\parallel}) + \tfrac{4}{3}\ell^3\xi^{\parallel}$$

and that substituting the parameters values to be calculated in Section 3.6 reveals the second term to be about four orders of magnitude larger than the first in the physical range of our problem. As such, we discard this first term and write $C_f = \frac{4}{3}\ell^3\xi^{\parallel}$ which will simplify our calculations greatly.

3.5 Non-Dimensionalisation

Seeking to identify key dimensionless parameters for our setup, we non-dimensionalise each of our dimensional quantities according to characteristic timescale T, length scale a and force scale F^{sp}. This gives

$$\hat{\mathbf{X}} = \mathbf{X}/F^{sp}, \qquad \hat{\mathbf{r}}_i = \mathbf{r}_i/a, \qquad \hat{t} = t/T$$

and hence $\frac{d}{d\hat{t}} = T\frac{d}{dt}$. Thus—abusing notation and omitting the $\hat{}$ on subsequent non-dimensionalised variables—we may rewrite (1), (2) and (3) as

$$\begin{aligned}
\dot{\mathbf{r}}_i &= \tfrac{T(-1)^{\delta_{if}}}{aA_i^{\perp}}(\mathbf{I} + (\alpha_i - 1)\mathbf{p}_i\mathbf{p}_i)\cdot(F^{sp}\mathbf{X} + \delta_{if}F^{sp}\mathbf{p}_f) \\
&= (-1)^{\delta_{if}}\tfrac{F^{sp}T}{a^2\eta}\frac{\eta a}{A_i^{\perp}}(\mathbf{I} + (\alpha_i - 1)\mathbf{p}_i\mathbf{p}_i)\cdot(\mathbf{X} + \delta_{if}\mathbf{p}_f) \\
&= (-1)^{\delta_{if}}\frac{R}{A_i^*}(\mathbf{I} + (\alpha_i - 1)\mathbf{p}_i\mathbf{p}_i)\cdot(\mathbf{X} + \delta_{if}\mathbf{p}_f) \qquad (4) \\
\dot{\theta}_i &= \tfrac{T}{C_i}((-1)^{\delta_{if}}\kappa(\theta_f - \theta_b) + (a_i\mathbf{p}_i \times F^{sp}\mathbf{X})\cdot\mathbf{n}) \\
&= \tfrac{F^{sp}T}{a^2\eta}\tfrac{a^3\eta}{C_i}(\tfrac{(-1)^{\delta_{if}}\kappa}{aF^{sp}}(\theta_f - \theta_b) + \tfrac{a_i}{a}(\mathbf{p}_i \times \mathbf{X})\cdot\mathbf{n}) \\
&= \tfrac{R}{C_i^*}((-1)^{\delta_{if}}\hat{\kappa}(\theta_f - \theta_b) + (\hat{\ell})^{\delta_{if}}(\mathbf{p}_i \times \mathbf{X})\cdot\mathbf{n}) \qquad (5) \\
\mathbf{r}_f &= \tfrac{1}{a}(a\mathbf{r}_b + a\mathbf{p}_b + \tfrac{\ell}{2}\mathbf{p}_f) \\
&= \mathbf{r}_b + \mathbf{p}_b + \hat{\ell}\mathbf{p}_f \qquad (6)
\end{aligned}$$

where our six key dimensionless groups are

$$R = \tfrac{F^{sp}T}{a^2\eta}, \qquad \hat{\kappa} = \frac{\kappa}{aF^{sp}}, \qquad \hat{\ell} = \frac{\ell}{2a},$$

$$\hat{\xi}^{\perp} = \frac{\xi^{\perp}}{\eta}, \qquad \hat{\xi}^{\parallel} = \frac{\xi^{\parallel}}{\eta}, \qquad e = \sqrt{1 - \frac{b^2}{a^2}}$$

Table 1: Ranges for physical parameters based on *V. alginolyticus*

Quantity	Value	Source
κ_{rlx}	$3.6(4) \times 10^{-26}\,\text{N m}^2$	Son et al. (2013)
κ_{ldd}	$2.2(4) \times 10^{-26}\,\text{N m}^2$	Son et al. (2013)
a	$1.60(25)\,\mu\text{m}$	Son et al. (2013)
b	$0.60(5)\,\mu\text{m}$	Son et al. (2013)
V	$47.1(88)\,\mu\text{m s}^{-1}$	Son et al. (2013)
P	$1.49(2)\,\mu\text{m}$	Xie et al. (2011)
r	$16\,\text{nm}$	Magariyama et al. (1995)
R_f	$140(20)\,\text{nm}$	Magariyama et al. (1995)
L	$4.59(100)\,\mu\text{m}$	Chattopadhyay & Wu (2009)

and the remaining coefficients in our governing equations are given by

$$A_b^* = \frac{A_b^\perp}{\eta a} = \frac{16\pi e^3}{(e^2+1)\ln(\frac{1+e}{1-e}) - 2e}, \qquad C_b^* = \frac{C_b}{a^3\eta} = \frac{32\pi e^3(2-e^2)}{3((e^2+1)\ln(\frac{1+e}{1-e}) - 2e)},$$

$$A_f^* = \frac{A_f^\perp}{\eta a} = 2\hat{\ell}\hat{\xi}^\perp \qquad C_f^* = \frac{C_f}{a^3\eta} = \frac{32}{3}\hat{\ell}^3\hat{\xi}^\parallel$$

which completely defines our system. Notably, the group R—an effective timescale, with force scaled by 'vulnerable time' of the hook in its numerator and viscous forces in its denominator—factors out of all differential equations in the system. This fact points to the role of R as a measure of the systems 'vigour', the strength and speed of its evolution over time. Note however that this parameter cannot be fully absorbed into the timescale without changing the dynamics of the system, due to the unwritten dependency of $\hat{\kappa}$ on T.

3.6 Parameter Calculations

In this subsection we generate reasonable ranges for our dimensionless parameters based on the literature surrounding *V. alginolyticus*. Directly citable values are listed in the following table. Inspection of Figure 1a in Son et al. (2013) suggests a range for T of 5 ms to 50 ms. Simulations in Section 5 will demonstrate that minimum alignment of the body (i.e. $\dot{\mathbf{r}}_b \cdot \mathbf{p}_b$) occurs between $t = T$ and $t = 2T$, so comparison with Figure 1d of Son et al. (2013) tightens this to 25 ms to 50 ms. A more detailed understanding of the hook's un/rolling will better inform this parameter choice. We can use helix geometry to calculate the length of the flagellum, namely $\ell = \frac{PL}{\sqrt{(2\pi R_f)^2+P^2}}$ where P, L, R_f are the pitch, contour length and radius of the helical flagellum respectively. We also calculate $\psi = \arctan\frac{2\pi R_f}{P}$ for use in calculation of the resistivities of the flagellum. To estimate the appropriate propulsive force magnitude F^{sp} we imagine the swimmer in perfect alignment, in which case no angular velocities or torques enter the calculations and the speed V of the swimmer is described by

$$V = \frac{F^{sp}}{A_b^\parallel + A_f^\parallel}$$

which can be compared with the known value for V to find F^{sp}. Note that this known value for V corresponds to bacteria swimming 'straight', but not with perfectly aligned components; we assume that the dynamics of this swimming are sufficiently close to perfectly straight swimming to make this calculation reasonable. Using these formulae and the resistivity values found in Section 3.4 we find

$$R \in (6.1, 87), \qquad \hat{\kappa}_{\text{ldd}} \in (0.16, 1.7), \qquad \hat{\ell} \in (0.78, 1.9),$$
$$\hat{\xi}^{\perp} \in (2.6, 4.0), \qquad \hat{\xi}^{\parallel} \in (4.6, 5.7), \qquad e \in (0.87, 0.96)$$

and additionally we calculate that $\hat{\kappa}_{\text{scl}} := \frac{\hat{\kappa}_{\text{rlx}}}{\hat{\kappa}_{\text{ldd}}} \in (0.011, 0.15)$. In all calculations to follow, dimensionless groups will be set to the median values of their ranges above, unless otherwise specified.

4 Dynamical Analysis

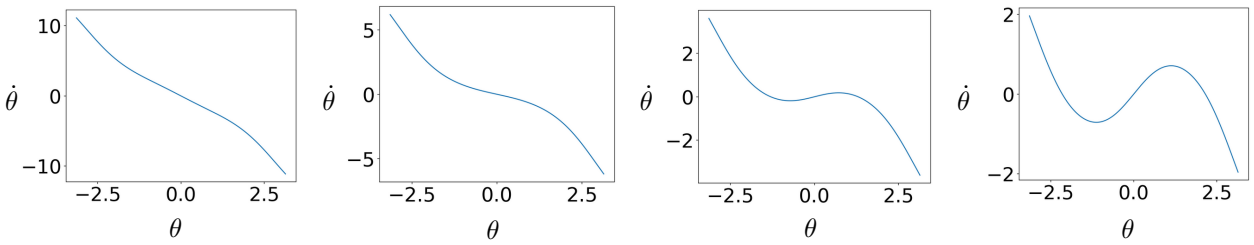

Figure 5: Values of $\dot{\theta}$ plotted numerically against θ. Left to right: $\kappa \approx 0.94,\ 0.52,\ 0.30,\ 0.17$ respectively.

In this section, we reduce our system to a one-dimensional dynamical system in terms of θ, and use linear stability analysis and simple techniques inspired by it to derive critical thresholds for $\hat{\kappa}$. In order to analyse our system, we first must simplify the system given by equations (4), (5) and (6) substantially.

Differentiating (6), we find $\dot{\mathbf{r}}_f - \dot{\mathbf{r}}_b = \dot{\mathbf{p}}_b + \hat{\ell}\dot{\mathbf{p}}_f$ which will assist us in eliminating (4); indeed substituting the expressions for $\dot{\mathbf{r}}_i$ allows us to solve for $\mathbf{X}$ in terms only of the θ_i and their derivatives, which we do symbolically using the SageMath mathematical computation package. Then substituting our newfound expression for $\mathbf{X}$ and solving for the derivatives $\dot{\theta}_i$ we reduce our system to a system of only two ODEs. Given these closed forms, we can completely describe the behaviour of the deflection-agnostic system with the difference $\dot{\theta} = \dot{\theta}_f - \dot{\theta}_b$. As might be expected, this expression can be simplified so as to depend only on θ and our non-dimensional groups; symbolic manipulation in SageMath delivers an explicit form for this derivative. Figure 5 contains graphs of this derivative against θ for various values of $\hat{\kappa}$. Note the single attractive fixed point of the system at $\theta = 0$ for higher values of κ, followed by pronounced nonlinearity at intermediate values and finally a pitchfork bifurcation (see Figure 6) of this fixed

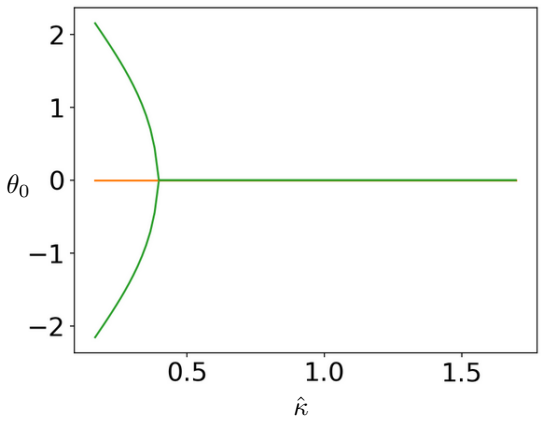

Figure 6: Fixed points θ_0 of θ against $\hat{\kappa}$.

point into an unstable fixed point surrounded on both sides by attractors. Using linear stability analysis around this fixed point, we derive the following expression for this critical value of $\hat{\kappa}$ at which this bifurcation occurs:

$$\hat{\kappa}_{\text{crit}} = \frac{\left(A_b^* A_f^* \hat{\ell}^2 - L A_f^* \hat{\ell} + C_f^* N\right) A_b^* \alpha_f}{\left(A_b^* A_f^* (\hat{\ell}+1)^2 + (C_b^* + C_f^*)(A_b^* + A_f^*)\right) M}$$

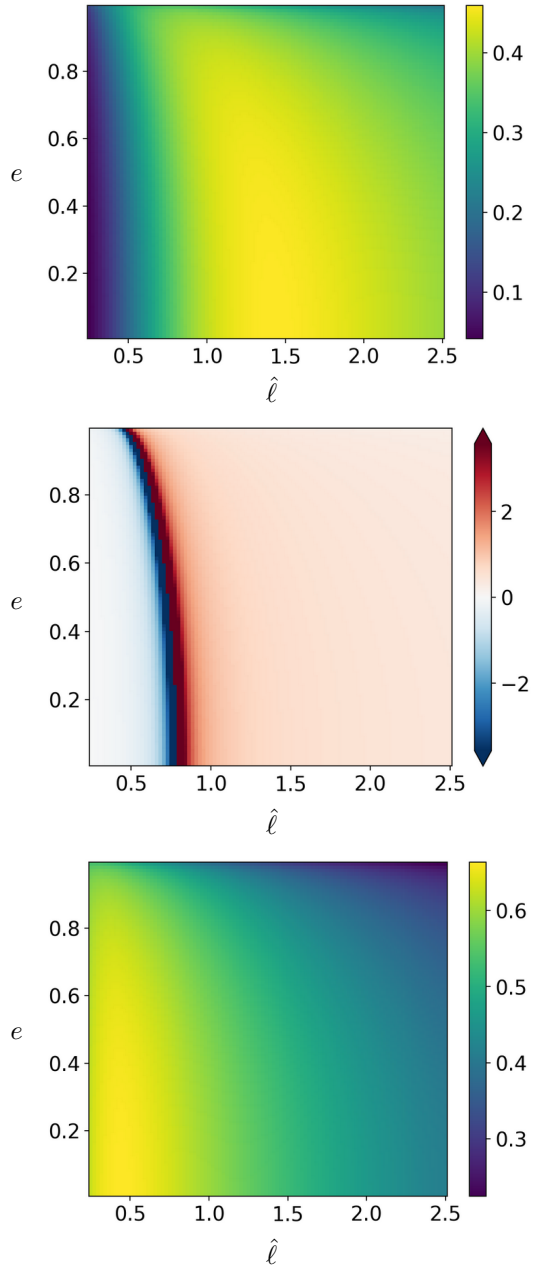

Figure 7: $\hat{\kappa}_{\text{crit}}, \hat{\kappa}_S$ and $\hat{\kappa}_b$ (top to bottom, respectively) against ℓ and e.

where $L = C_b^* \alpha_b - A_b^* - C_b^*$, $M = A_f \alpha_b + A_b \alpha_f$ and $N = A_f \alpha_b + A_b$ are simplifying parameters that depend only on e, $\hat{\xi}^{\perp}$ and $\hat{\xi}^{\parallel}$. Graphs of this parameter for various values of $\hat{\ell}$ and e are included in Figure 7; flagellar resistivity parameters have negligible impact on its value.

This critical threshold separates totally buckled swimming from straight swimming for a static-stiffness swimmer, but does not fully govern behaviour for microswimmers with dynamically stiffening flagellar hooks; parameter calculations in Section 3.6 suggest that both the behaviours governed by subcritical and supercritical parameter sets are both observed within each flick. As such, we seek other quantities that can describe the modality of the hook. Let us define $S = \theta_f + \theta_b$, twice the mean orientation angle of the swimmer. We might expect also that $\dot{S} = \dot{\theta}_b + \dot{\theta}_f$ is expressible in terms of θ alone; indeed symbolic manipulation again confirms this to be the case. For high $\hat{\kappa}$, $\dot{S} > 0$ when $\theta > 0$—meaning that realignment favours the direction of θ_f—but for low $\hat{\kappa}$ the opposite is true. Thus performing a similar linearisation yields the critical value

$$\hat{\kappa}_S = \frac{\left(A_b^* A_f^* \hat{\ell}^2 + L A_f^* \hat{\ell} + C_f^* N\right) A_b^* \alpha_f}{\left(A_b^* A_f^* (\hat{\ell}^2 - 1) + (C_f^* - C_b^*)(A_b^* + A_f^*)\right) M}$$

which (as shown in Figure 7) possesses a singularity that aligns well with the low-$\hat{\kappa}_{\text{crit}}$ region's border. The consistently larger value of $\hat{\kappa}_S$ compared to $\hat{\kappa}_{\text{crit}}$ to the 'right' of this singularity demonstrates the existence of a regime in which microswimmers swim in stable, overdamped trajectories but nevertheless favour the direction of the head in their return to equilibrium. Finally by noting $\dot{\theta}_b = \frac{\dot{S} - \dot{\theta}}{2}$, we may derive an expression for $\dot{\theta}_b$ in terms of only θ, and yet another critical value for its buckling given by

$$\hat{\kappa}_b = \frac{\left(A_b^* A_f^* \hat{\ell}^2 + C_f^* N\right) A_b^* \alpha_f}{\left(A_b^* A_f^* (\hat{\ell}^2 + \hat{\ell}) + C_f^* (A_b^* + A_f^*)\right) M}$$

that dictates whether θ_b will migrate towards or away from θ_f in the system's return to equilibrium. Numerical values of $\hat{\kappa}_b$ are visible in Figure 7. Note the intermediate value of $\hat{\kappa}_b$ when compared with $\hat{\kappa}_{\text{crit}}$ and $\hat{\kappa}_S$; behaviour ranges qualitatively from favouring flagellar angle, to favouring body angle, to keeping the body still/moving it away from the flagellum, to remaining buckled throughout. The mode bounded by $\hat{\kappa}_{\text{crit}}$ and $\hat{\kappa}_b$ is likely the most crucial physical range; because the total reorientation time of the swimmer is often longer than $4T$, the direction of body movement in response to angle deflection at $\hat{\kappa}_{\text{ldd}}$ represents the relevant regime for most of the reorientation event, and thus semi-buckled behaviour in this domain is crucial to achieving large final deflection while still returning to equilibrium.

5 Swimmer Trajectories

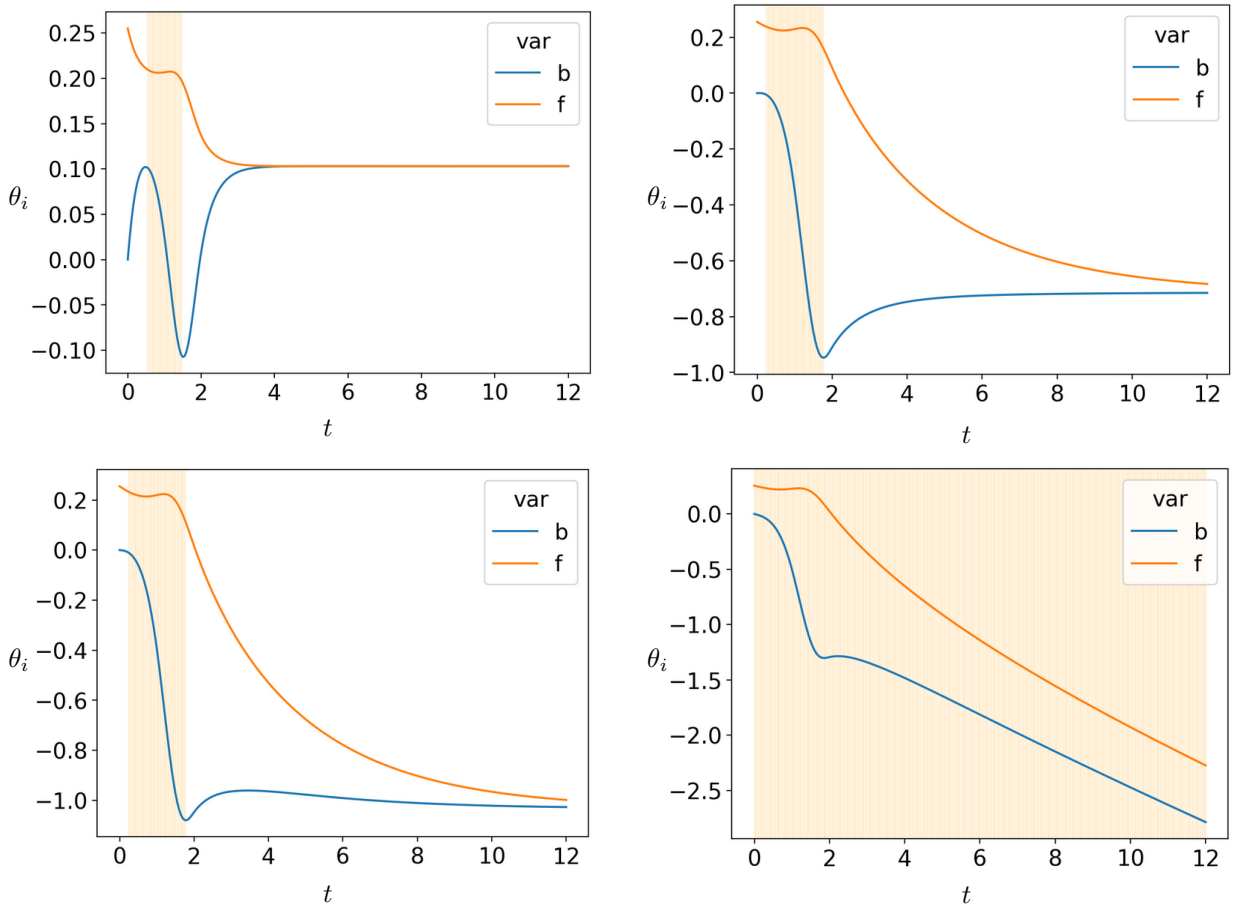

Figure 8: Numerically solved trajectories of θ_i against t. Regions marked with yellow bars represent $\hat{\kappa} < \hat{\kappa}_{\text{crit}}$. Left to right, top then bottom: $(\hat{\kappa}, \hat{\ell}) = (0.93, 1.10),\ (0.47, 1.10),\ (0.47, 1.00),\ (0.40, 1.00)$ respectively.

We proceed now to solve our two-dimensional system of ODEs derived in Section 4 using a backwards differentiation formula (BDF) method implemented in SciPy. For initial conditions, we consider a small but positive initial value of θ to perturb the system, expressed without loss of generality as $\theta_b = 0, \theta_f = \theta$. Figure

8 contains graphs of the trajectories of the θ_i for $t \in [0, 8]$, which are representative of the main behavioural regimes observed in simulations. Foremostly, for $\hat{\kappa}_{\text{ldd}} > \hat{\kappa}_S$, angle sum (and thus average angle) favours the direction of θ_f. As such, despite the 'buckled' behaviour displayed by the system in the subcritical region of such trajectories—which sees the angle sum grow rather than shrink—both angles eventually realign favouring the positive direction. This is physically realised as a brief shake of the swimmer's head, but ultimately a final trajectory well aligned with the initial value of θ_f, as showcased in the top left of Figure 8. Alternatively, for $\hat{\kappa}_{\text{ldd}} < \hat{\kappa}_S$, angle sum favours the direction of the body even while the flagellar hook is fully loaded. Because the loaded period can often extend far longer than 2 units of non-dimensional time, this greatly affects final deflection angle, allowing for substantial 'flicks' in the opposite direction to initial perturbation, as demonstrated in the top right of Figure 8. When $\hat{\kappa}_{\text{ldd}}$ nears or surpasses $\hat{\kappa}_b$, $\dot{\theta}_b$ is either slightly negative or very near zero for small values of θ. This 'steady body' behaviour is demonstrated by the bottom left trajectory in Figure 8, which (unlike the similar trajectory in the top right) demonstrates decreasing θ_b even in the unbuckled region. Finally, for $\hat{\kappa}_{\text{ldd}} < \hat{\kappa}_{\text{crit}}$, the swimmer exists only in an underdamped, 'buckled' configuration reminiscent of the helical trajectories from Nguyen & Graham (2017). Characteristic trajectories for overdamped, underdamped and flick regimes are animated online as supplementary material.

6 Final Deflection

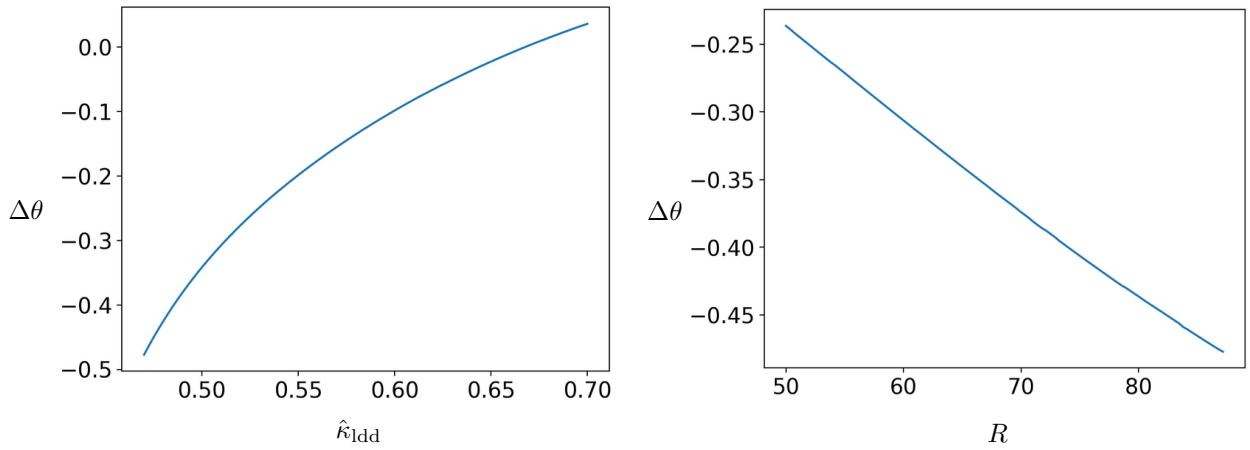

Figure 9: Left: $\Delta\theta$ against $\hat{\kappa}_{\text{ldd}}$, for $\theta_{\text{init}} = 0.255$ and $R = 87$. Right: $\Delta\theta$ against R, for $\theta_{\text{init}} = 0.255$ and $\hat{\kappa}_{\text{ldd}} = 0.47$

Here we describe the effect of our parameters on the overall turn angle. In Figure 9 we can see the relationship between final deflection angle (that is, the final of θ_b at the final timestep of a numerical simulation) and the parameters R and $\kappa\hat{\text{ldd}}$. Across all simulations, R has a simplistic (nearly linear) relationship with $\Delta\theta$, positively correlated with $\Delta\theta$. The effect of varying R is notably less strong than that of varying $\hat{\kappa}_{\text{ldd}}$, suggesting the potential for R to 'fine tune' the deflection angle i.e. make small adjustments to $\Delta\theta$ to assist with chemotaxis. Also elucidated in Figure 9 is the key role of $\hat{\kappa}_{\text{ldd}}$ in determining final angle deflection. Though $\Delta\theta$ is highly

dependent on $\hat{\kappa}$, the relationship between these quantities is markedly nonlinear; it demonstrates a flat gradient in the $\hat{\kappa}_{\text{ldd}} > 0.55$ region that tapers below this threshold. This shape is universal across different values of $\hat{\ell}$, but the range of $\Delta\theta$ spanned for shorter flagella, which we explain with reference to Figure 10.

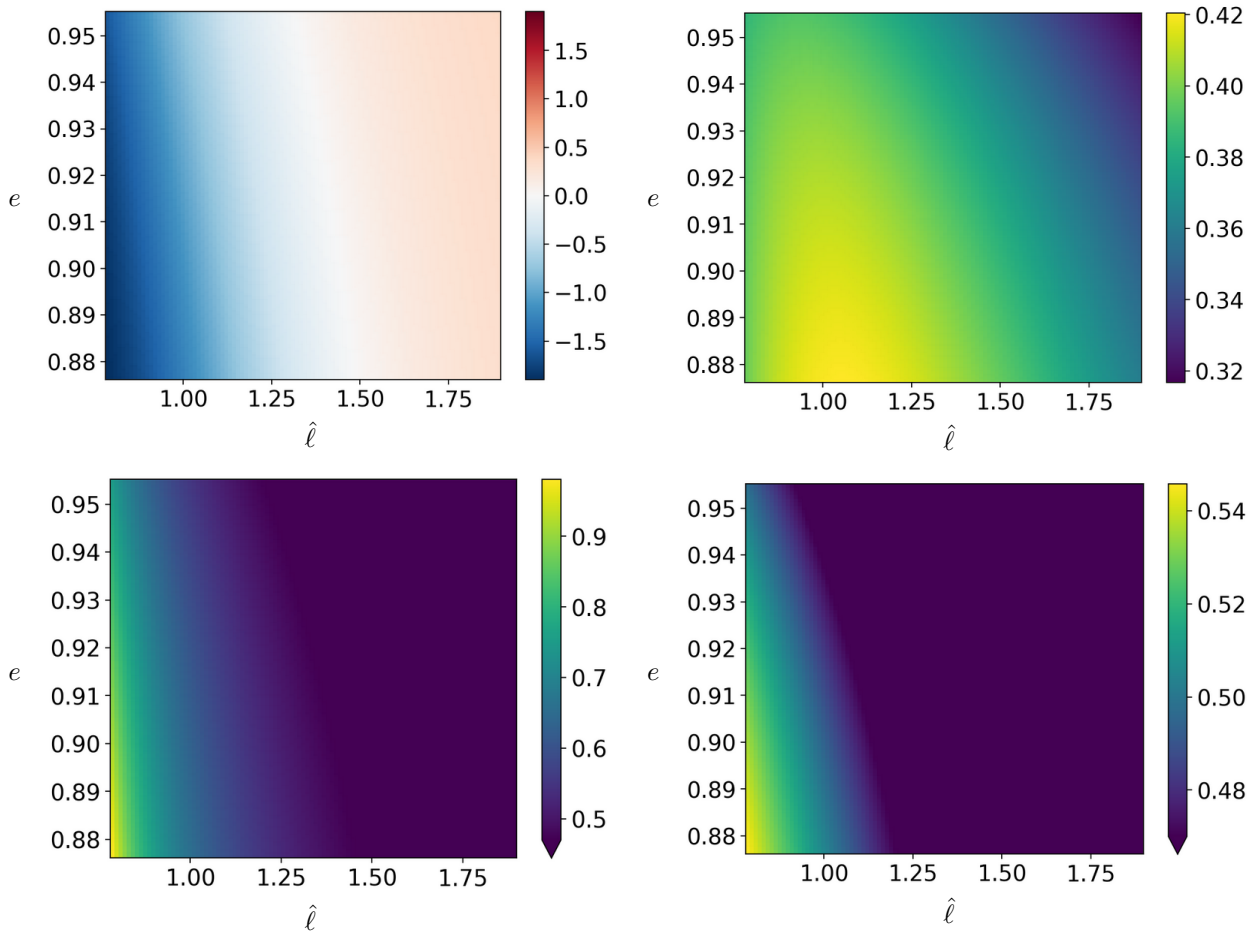

Figure 10: $\Delta\theta$ compared with critical parameters, for physical range of $\hat{\ell}$ and e. Top left: $\Delta\theta$, for $\theta_{\text{init}} = 0.5$, $\hat{\kappa}_{\text{ldd}} = 0.47$. Top right: $\hat{\kappa}_{\text{crit}}$. Bottom left: $\hat{\kappa}_S$, values above 0.47. Bottom left: $\hat{\kappa}_b$, values above 0.47.

We can see that the relationships between deflection angle and $\hat{\ell}$or e are best understood through the effects of these parameters on critical values of $\hat{\kappa}$, which is the primary determinant of deflection angle; comparison of the $\hat{\kappa}_S$ and $\hat{\kappa}_b$ panels with the $\Delta\theta$ panel reveals good agreement between the $\hat{\kappa}_S = 0.47$ and the beginning of the $\Delta\theta < 0$ region, and between $\hat{\kappa}_b = 0.47$ a sharp increase in $\Delta\theta$. Interestingly, $\hat{\kappa}_{\text{crit}}$ does not well predict regions of parameter space corresponding to large $\Delta\theta$ for non-underdamped swimmers; we interpret this as a result of the longer period spent by the swimmer in the fully loaded state as compared to the short subcritical period. We finally speak briefly to the effect of θ_{init} on eventual $\Delta\theta$, shown in Figure 11. For large $\hat{\ell}$, this relationship is effectively linear, with final angle just over half of initial angle. However, as $\hat{\ell}$ lessens, this relationship develops a minimum that moves rightwards from $\theta_{\text{init}} = 0$. Finally in the extreme case of low $\hat{\ell}$, the gradient in the high θ_{init} region flattens out greatly. This final regime can be thought of as having a near-independence of $\Delta\theta$ from

θ_{init}, once the latter is large enough to overcome the initial 'startup' angle required.

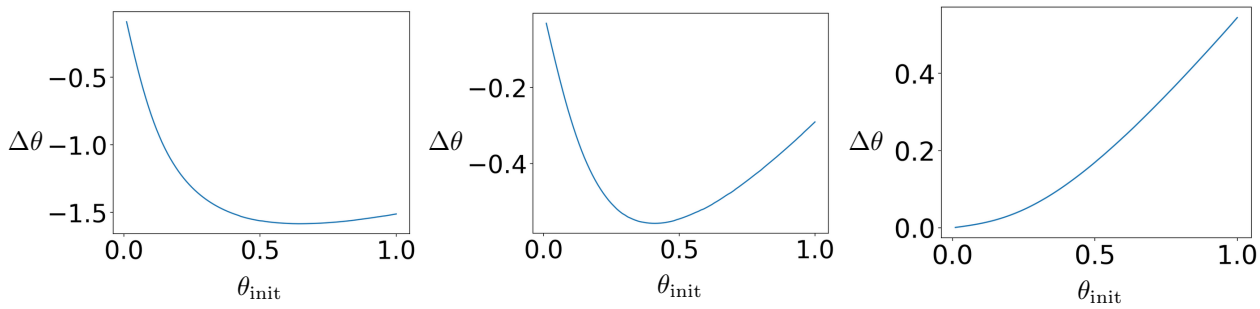

Figure 11: $\Delta\theta$ against θ_{init}, for $\hat{\kappa}_{\text{ldd}} = 0.47$. Left to right: $\hat{\ell} = 0.79,\ 1.10,\ 1.58$.

7 Discussion and Conclusion

This work has introduced a simplified model for the trajectories of microswimmers with flexible flagellar hooks that stiffen and soften over time, and successfully modelled some key qualities of the flick component of run-reverse-flick motility. As in previous work, a key dimensionless group $\hat{\kappa}$ that balances hook stiffness against propulsive force was identified, in addition to a new timescale group R with a simple proportional relationship to final flick angle. Furthermore, length ratio $\hat{\ell}$ between flagellum and cell head was identified as a key determinant of swimming modes due to its affect on critical buckling thresholds for this force ratio. The former two parameters, due to their dependence on propulsive force and hook unrolling time, could plausibly vary within a single specimen (Magariyama et al. (1995)) highlighting their possible role in the angle variation observed by Son et al. (2013) and thus as key drivers of chemotaxis. Contrastingly, the ratio between flagellar and body length is known (Magariyama et al. (1995)) to vary significantly within a single species. This fact suggests the potential for length ratio to contribute to varied behaviour within a population, which may positively effect species viability.

The highly idealised propulsion mechanism utilised by this model does ultimately pose significant limitations to its scope. In particular, it reduces the problem to that of a one-dimensional dynamical system, which is a substantial simplification; under these conditions, the bacterial flagellum is unable to cross the equilibrium angle as is observed in Son et al. (2013). Certainly, then, a natural next step for further research is the extension of this dynamic stiffening concept to a full three dimensional model with a helical flagellum, as is studied in Nguyen & Graham (2017). Finally, detailed modelling of the hook based on research by Nord et al. (2022) will provide the necessary context to evaluate the validity of this study's dynamic stiffening relationship.

8 Acknowledgements

This work was supported by a Summer Research Scholarship from the Australian Mathematical Sciences Institute. I thank A/Prof Douglas Brumley of The University of Melbourne for his supervision and guidance.

References

Chattopadhyay, S. & Wu, X. L. (2009), 'The effect of long-range hydrodynamic interaction on the swimming of a single bacterium', *Biophysical Journal* **96**, 2023–2028.

Jabbarzadeh, M. & Fu, H. C. (2018), 'Dynamic instability in the hook-flagellum system that triggers bacterial flicks', *Physical Review E* **97**.

Kato, T., Makino, F., Miyata, T., Horváth, P. & Namba, K. (2019), 'Structure of the native supercoiled flagellar hook as a universal joint', *Nature Communications* **10**.

Kim, S. & Karrila, S. J. (1991), *Microhydrodynamics : principles and selected applications*, Butterworth-Heinemann.

Koike, M., Terashima, H., Kojima, S. & Homma, M. (2010), 'Isolation of basal bodies with c-ring components from the na +-driven flagellar motor of vibrio alginolyticus'.

Lauga, E. & Powers, T. R. (2008), 'The hydrodynamics of swimming microorganisms'.
URL: *http://arxiv.org/abs/0812.2887 http://dx.doi.org/10.1088/0034-4885/72/9/096601*

Lighthill, J. (1976), Flagellar hydrodynamics* the john yon neumann lecture, 1975, Technical report.
URL: *http://www.siam.org/journals/ojsa.php*

Magariyama, Y., Sugiyama, S., Muramoto, K., Kawagishi, I., Imae, Y. & Kudot, S. (1995), Simultaneous measurement of bacterial flagellar rotation rate and swimming speed, Technical report.

Nguyen, F. T. & Graham, M. D. (2017), 'Buckling instabilities and complex trajectories in a simple model of uniflagellar bacteria', *Biophysical Journal* **112**, 1010–1022.

Nord, A. L., Biquet-Bisquert, A., Abkarian, M., Pigaglio, T., Seduk, F., Magalon, A. & Pedaci, F. (2022), 'Dynamic stiffening of the flagellar hook', *Nature Communications* **13**.

Purcell, E. M. (1977), 'Life at low reynolds number', *American Journal of Physics* **45**.

Qiu, T., Lee, T. C., Mark, A. G., Morozov, K. I., Münster, R., Mierka, O., Turek, S., Leshansky, A. M. & Fischer, P. (2014), 'Swimming by reciprocal motion at low reynolds number', *Nature Communications* **5**.

Son, K., Brumley, D. R. & Stocker, R. (2015), 'Live from under the lens: Exploring microbial motility with dynamic imaging and microfluidics'.

Son, K., Guasto, J. S. & Stocker, R. (2013), 'Bacteria can exploit a flagellar buckling instability to change direction', *Nature Physics* **9**, 494–498.

Sourjik, V. & Wingreen, N. S. (2012), 'Responding to chemical gradients: Bacterial chemotaxis'.

Takano, Y., Yoshida, K., Kudo, S., Nishitoba, M. & Magariyama, Y. (2003), 'Takanoetal-smalldeformationofvibrioflagella', *JSME International Journal Series C* **46**.

Xie, L., Altindal, T., Chattopadhyay, S., Wu, X.-L. & Berg, H. C. (2011), 'Bacterial flagellum as a propeller and as a rudder for efficient chemotaxis', **108**, 2246–2251.